Bioinspired Gradient Covalent Organic Framework Membranes for Ultrafast and Asymmetric Solvent Transport

Hongyu Zuo [1], Baokang Lyu [1], Jiaao Yao [1], Wenhua Long [1], Yu Shi [1], Xinghao Li [1], Huawei Hu [1], Arne Thomas [2], Jiayin Yuan [3], Bo Hou [4], Weiyi Zhang [1], Yaozu Liao [1]**

H. Y. Zuo, B. K. Lyu, J. A. Yao, W. H. Long, Y. Shi, X. H. Li, H. W. Hu, W. Y. Zhang, Y. Z. Liao

State Key Laboratory for Modification of Chemical Fibers and Polymer Materials, College of Materials Science and Engineering, Donghua University Shanghai 201620 China

Weiyi Zhang (email: wyzhang@dhu.edu.cn) & Yaozu Liao (email: yzliao@dhu.edu.cn)

Arne Thomas

Technische Universität Berlin, Department of Chemistry, Functional Materials, Sekretariat BA 2, Hardenbergstr. 40, 10623 Berlin

J. Y. Yuan

Department of Materials and Environmental Chemistry, Stockholm University, Stockholm 10691, Sweden

B. Hou

School of Physics and Astronomy, Cardiff University, Queen's Building, The Parade, Cardiff, Wales CF24 3AA, United Kingdom

Keywords: Bioinspired; Gradient Covalent Organic Framework Membrane; Asymmetric Solvent Transport

Gradients played a pivotal role in membrane technologies, *e.g.*, osmotic energy conversion, desalination, biomimetic actuation, selective separation and more. In these applications, the compositional gradients are of great relevance for successful function implementation, ranging from solvent separation to smart devices. However, the construction of functional gradient in

membranes is still challenging both in scale and directions. Inspired by the specific function-related, graded porous structures in glomerular filtration membranes, we report here a general approach for constructing gradient covalent organic framework membranes (GCOMx) applying poly (ionic liquid)s as template. With graded distribution of highly porous COF crystals along the membrane, GCOMx exhibited an unprecedented asymmetric solvent transport when applying different membrane sides as the solvent feed surface during filtration, leading to a much-enhanced flux (10~18 times) of the "large-to-small" pore flow comparing to the reverse direction, verified by hydromechanical theoretical calculations. Upon systematic experiments, GCOMx achieved superior permeance in nonpolar (hexane~260.45 LMH bar^{-1}) and polar (methanol~175.93 LMH bar^{-1}) solvents, together with narrow molecular weight cut-off (MWCO, 472 g mol^{-1}) and molecular weight retention onset (MWRO, <182 g mol^{-1}). Interestingly, GCOMx showed significant filtration performance in simulated kidney dialysis, revealing great potential of GCOMx in bionic applications.

1. Introduction

Precedents of filtration membranes with graded structures/functions can be found in natural living organisms like leaf cuticles[1] or glomerular filtration membranes.[2] For instance, the biological filtration membranes on kidney tubules in renal glomerulus with a multilayer graded porous structures embedded inside, can filtrate the blood and remove small molecules (incl. mineral, glucose, uric acid, urea, *etc*.) selectively and efficiently.[3] With large sparse pores near the blood flow and small dense pores discharging the filtrate wastes, the high-performing glomerular filtration membranes can filtrate flowing blood and generate initial urine with a glomerular filtration rate (GFR) of 3.05-6.03 L h^{-1} m^{-2} [4] through renal follicle while reserving protein and blood cells.[5, 6] However, artificial graded filtration membranes are rarely described nor thoroughly studied, except a few pioneering works[7-9] with potentials in solvent transport and molecule rejection. The implantation of such a design motif into synthetic functional

materials would yield a plethora of practical applications in engineering and biomedical fields, *e.g.* for bionic actuators[10] or power generation[11] Thus, with graded distributed sizes/densities of pores, nano-porous membranes are expected to exhibit biomimetic features such as narrow molecular sieving, mechanical robustness and/or significant solvent permeance, similar to glomerular filtration membranes or like bamboo vascular bundles[12] and wood branched fiber structures.[13] Furthermore, the internal structure-function relationships of compositional graded membranes are largely unknown. Consequently, an in-depth investigation on the relationship between their gradient and function is highly desirable for membrane technologies, especially in filtration and separation.

Covalent organic frameworks (COFs), as a class of crystalline porous materials featuring tunable ordered structures, are constructed from two or three dimensional (2D/3D) building blocks through covalent linkages.[14] Recently, COFs have emerged as promising materials for various applications , such as adsorbents,[15] in catalysis,[16] for energy storage[17] or chemical sensors,[18, 19] owing to their adjustable pore sizes, well-defined channels, versatile and tunable functionalities. Due to their highly aligned nanopores,[20] also called single-digit nanopores (SDNs), COFs showed potential in separation applications.[21, 22] For example, some ultrathin COF membranes with tunable aperture[23] can surpass conventional separation materials.[24] However, although powdery COFs normally possess large surface areas, tuneable pore sizes/structures along with tailorable functionalities, most these features cannot be simply inherited by their membrane derivatives because of the inevitable defects in COF's rigid skeleton on a large scale. Consequently, the fabrication of macroscale COF membrane is facing significant challenges.[25] I) poor crystallinity/inevitable defects in macroscale; II) low chemical stability as membranes; III) mechanical weakness in a membrane state; IV) restrained functionalities derived from low processabilities. These drawbacks can reduce the solvent permeance and accuracy of rejection. Accordingly, a universal construction route for large area COF membranes is of great necessity.

Inspired by the graded porous structure observed in the glomerular membrane, we report here a general synthetic strategy to fabricate gradient covalent organic framework membranes (GCOMx) integrated with imidazolium-based poly(ionic liquid)s (PILs) (Figure 1a-b).[26] An *in-situ* growth method was conducted to construct the GCOMx by applying pre-synthesized porous poly(ionic liquid) membranes as template, with COF crystals generated from graded distributed precursors (2,5-diamino-1,4-phenyl-dicarboxylic acid, DAPAC) inside the PIL membrane (PIL-M) (Figure 1c-d). Owing to the graded electrostatically crosslinking feature, PIL membrane was chosen as one powerful platform for constructing gradient COF crystals along the membranes' cross-sectional direction. The GCOMx exhibited good mechanical stability, high crystallinity and excellent permeation for organic solvents including methanol, ethanol, 1-propanol, isopropanol and hexane. Unprecedently, asymmetric solvent permeations were detected for GCOMx when different feed surfaces of the membrane were applied for crossflow filtration. Evidenced by theoretical calculations and confirmed by practical experiments, it is convinced that, when applying the membrane surface with the large and sparse pores/fewer COF crystals as the solvent feed side, an enhanced solvent permeance (10~18 times) than the reverse operation can be achieved. Based on this discovery, organic solvent nanofiltration (OSN) was performed with GCOMx, realizing top-ranked methanol and hexane permeation in OSN (175.93 LMH bar^{-1} and 260.45 LMH bar^{-1}) for porous organic polymer (POP) membranes.[27] Additionally, GCOMx achieved one of the best molecular weight cut-off (MWCO) and molecular weight retention onset (MWRO) of 472 g mol^{-1} and <182 g mol^{-1} among COF membranes. Calculated by molecular dynamics and finite element fluid dynamics simulation, the pore channels of GCOMx possess an excellent molecular sieving ability, with mean-squared displacement (MSD) order of $MSD_{methanol} > MSD_{ethanol} > MSD_{1\text{-propanol}}$. Furthermore, in order to demonstrate the practical usage of the membranes, mixed drugs separation and simulated kidney dialysis were tested for GCOMx, resulting in highly effective filtration and asymmetric solvent retention.

2. Preparation of the GCOMx

Prior to the fabrication of GCOMx, the gradient porous PIL-M were constructed following a previous report.[28] The chemical synthesis started with a PIL-poly[3-cyanomethyl-1-vinyl-imidazolium bis(trifluoromethane sulfonyl)imide] (termed "PImi," chemical structure shown in Figure S1a), which carries a cyanomethyl substituent along its polyimidazolium backbone. Its chemical structure and apparent molecular weight was characterized and confirmed by proton nuclear magnetic resonance (^{1}H NMR) spectroscopy and gel permeation chromatography (Figure S1b-c). Subsequently, a homogeneous solution of PImi and diamino-phenyl dicarboxylic acid (DAPAC) (molar ratio of cation:COOH=1:1) in *N*,*N*-dimethylformamide (DMF) was made and cast onto a glass plate, followed by solvent removal (80 °C, 2 h) to produce a sticky blend polymer film, *i.e.* PImi-F. The PImi-F on the glass plate was then immersed into a NH_3 solution (aq. 0.25 wt%) for 2 h to induce an *in-situ* electrostatic complexation (EC) between DAPAC and surrounded PImi chains to build up an electrostatically cross-linked porous membrane (pore formation mechanism in Figure S2) (Note: the membrane surface in direct contact with the NH_3 solution during formation process is termed as ''Top surface'', while the other side in contact with the vessel plate is termed as ''Bottom surface''). The as-formed PIL-M can be easily peeled off from the glass plate. The resultant membrane contained a gradient profile in both the cross-linking density and DAPAC distribution along the cross-section of the membrane (Figure S2). The differences in cross-linking density/DAPAC distribution are owing to the diffusive penetration of ammonia into the polymer membrane on the glass substrate and being highest on the Top and lowest at the Bottom. Consequently, based on the DAPAC distribution gradient, graded distributed imine-type COF crystals were generated *in-situ* from porous PIL-M templates (Figure S2), through a heterogeneous nucleation methodology with DAPAC as the nucleation agent during COF formation.[29,30] Following this approach, three GCOMx (x=1,2,3) were prepared *via* reacting para-phenylenediamine (PDA) with triformyl-benzenes (1,3,5-triformylphloroglucinol (TFP),

1,3,5-triformylbenzene (TFB) and 1,3,5-tris-(4-formyl-phenyl)triazine (TFPT)), respectively. The obtained highly crystalline COFs are named COF-TpPa, COF-LZU1, COF-NUS14 according to previous reports (Figure S3-5).[31-33] The graded distribution of COF crystals along the cross-sections of GCOMx are proved by iodine vapor adsorption experiment (Figure S6) and subsequent elemental line scan *via* scanning electron microscopy (SEM) with energy-dispersive X-ray spectroscopy (EDS) (Figure 1c, Table S1). Besides, the cyanomethyl group attached to the imidazolium moiety in PImi can be partially hydrolyzed into aminoethyl group ($-C_2H_4-NH_2$), which can further react with aldehyde moieties to form imines and thus act as covalent anchor point for COF crystal growth (Figure 1d).

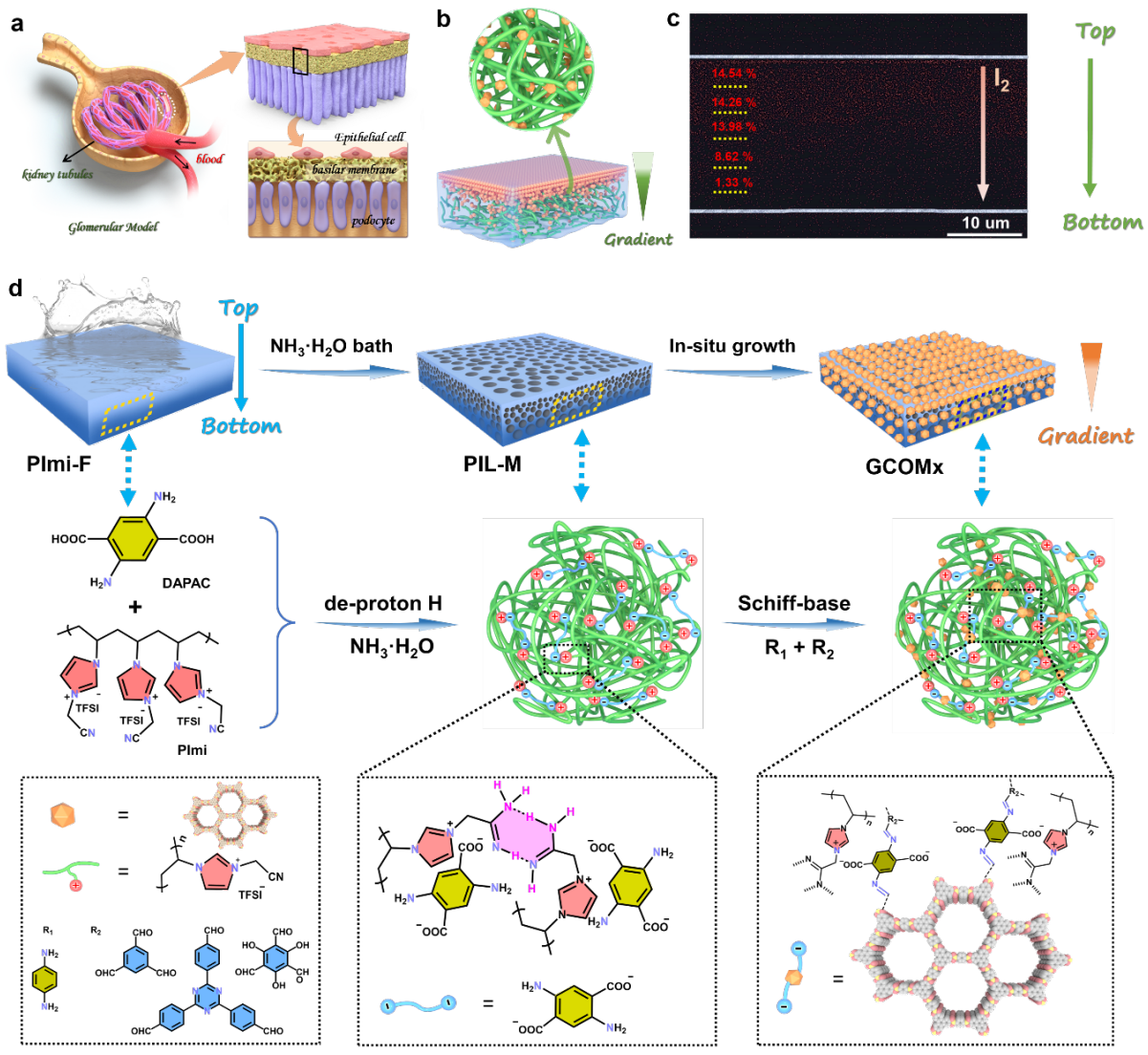

Figure 1. Scheme of the bioinspired structure of GCOMx and the general synthetic route. **a** Simplified human kidney model; **b** Model of gradient covalent organic framework membranes; **c** The cross-sectional elemental mapping and line scan of iodine distribution in GCOM1 by SEM with EDS after adsorbing iodine vapor; **d** Schematic synthetic route for GCOMx. (Left: the formation of porous PIL-M from electrostatic complexation triggered by $NH_3{\cdot}H_2O$ bath; Middle: electrostatic complexation between PImi and DAPAC, hydrogen bond networks formed *via* partially hydrolyzed cyanomethyl group; Right: *in-situ* COF crystal growth applying DAPAC as the nucleation agent).

2. Characterization Techniques of the GCOMx

To gain further insight into the morphology of as-fabricated membranes, scanning electron microscopy and atomic force microscopy (AFM) are used to elucidate their thicknesses, cross-section, surface morphologies and roughness. As shown in Figure S7, the PIL-M exhibited a uniform planar shape and a dark red color. SEM images showed that the Top surface of the PIL-M is smooth, while the Bottom surface is wrinkled, with a membrane thickness of ~31 μm. A graded pore size distributions along the membrane can be identified by the cross-sectional SEM pictures (Figure S8a). Specifically, the pores were smaller (20~45 nm in size) on the Top side of the membrane and gradually increased to 0.1~0.4 μm toward the Bottom side (Figure S8b-d). Such PIL-M can be subsequently processed into large-scale composite membranes (*i.e.* GCOMx) *via in-situ* growth of COF nanoparticles. As shown in the optical images, three GCOMx, *i.e.* GCOM1, GCOM2, and GCOM3 were obtained when COF-TpPa, COF-LZU1, and COF-NUS14 were applied, respectively (Figure 2, Figure S9). The membrane thickness values are measured to be 32.6±0.1 μm, 37.9±0.6 μm and 39.1±0.5 μm for GCOMx (x=1,2,3) (Figure 2). Low magnified SEM images (×3.5 K) show a continuous COF layer with well-intergrown grains of the COFs formed on the Top surface of the membrane (Figure 2a-c). Additionally, the Top and Bottom surfaces of GCOM1, GCOM2, and GCOM3 are obviously different (Figure S10). The dense layer formed by continuous COF nanoparticles on the Top surface of the membranes exhibited uniform and densely-packed morphologies, as shown in

their close-view SEM images (Supplementary Figure11-13, ×20 K). On the contrary, plentiful defects and flaws can be observed at the Bottom surface of the membranes, owing to the membrane demolding and phase separations. A close inspection of 2D/3D AFM images further disclosed the surface morphologies of GCOMx. The average roughness (Ra) of both GCOM1 and GCOM3 are lower than 15 nm (Figure 2 and Figure S14), while the average roughness (Ra) of GCOM2 is more than 100 nm due to the larger nanoparticle size resulted from COF-LZU1 (Figure S11). The surface roughness of the PIL-M can also be discerned from magnified 2D/3D AFM images (Figure S15). Alternatively, as shown in Figure 2, the cross-sections of GCOMx are hierarchically porous, with the pore channels ranging from small and dense (Top) to large and sparse (Bottom). With observations from SEM images, it can be speculated that a graded distribution of COF nanoparticles with a decreasing particle density from Top to Bottom side of the membranes is formed (Figure S16-18). Since higher density of COFs absorb more iodine molecules, such gradients can be directly observed *via* iodine vapor adsorbing experiments using GCOMx as the adsorbents. For comparison, the iodine adsorption of PIL-M without COF nanoparticles was also conducted (Figure S6). For the experiments, the membranes were quickly placed into the I_2 vapor atmosphere as a whole piece and lasted for 90 min, after that, Interestingly, no gradient iodine distribution was observed in the EDS line scan of PIL-M cross-section (Figure S19). On the contrary, obvious graded adsorbed I_2 (Figure 1c, Figure S20 and Table S1) were observed in the SEM-EDS line scan/mapping images for GCOMx, confirmed the graded distribution of COF crystals along the membrane cross-sections.

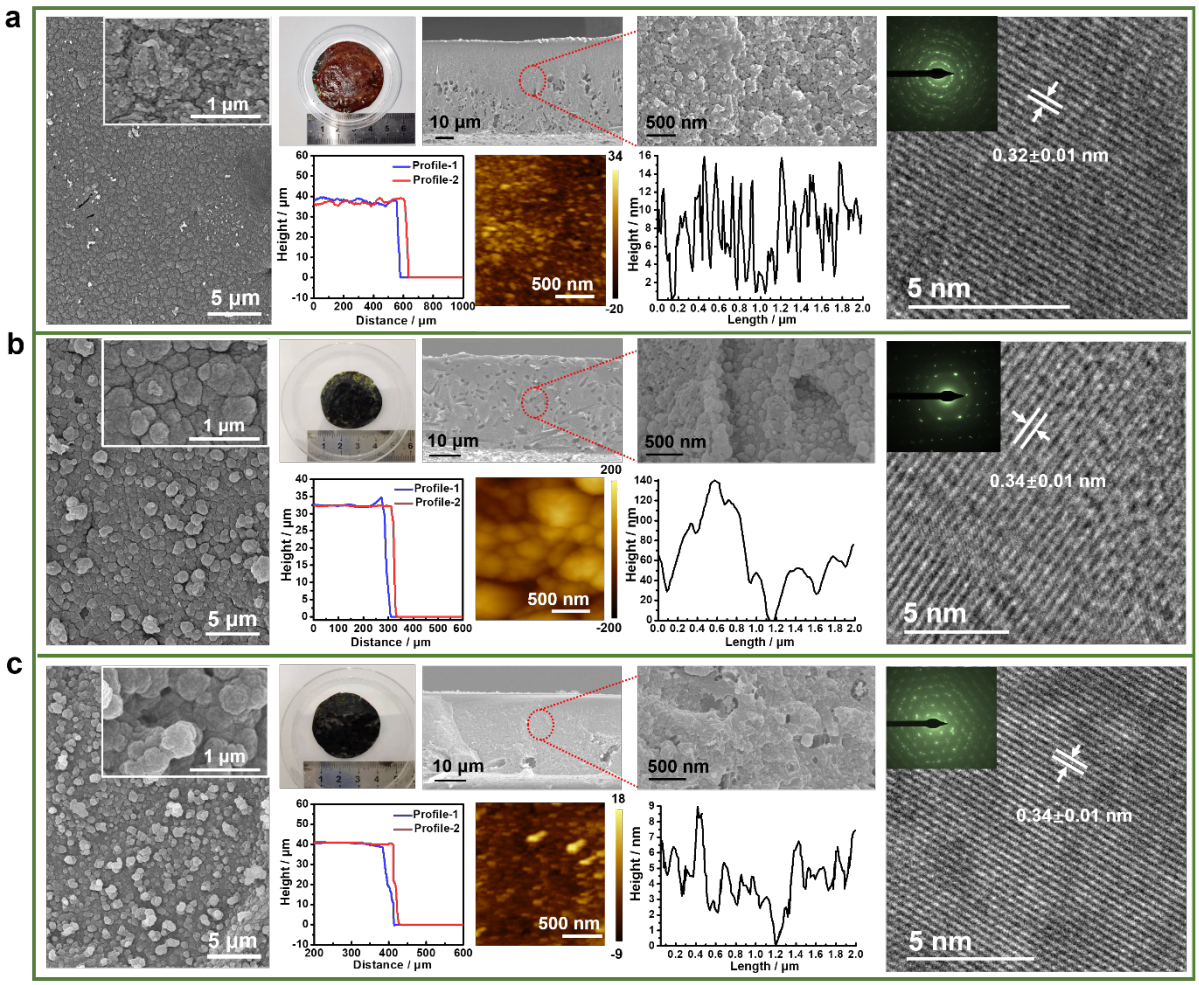

Figure 2. Morphology characterization of GCOMx. a-c The surface morphological SEM images of GCOMx illustrated in the left column; Optical images, cross-sectional SEM images, thickness and AFM images of the GCOMx illustrated in the middle column; TEM images and selected-area electron diffraction patterns of the GCOMx illustrated in the right column.

The high crystallinity of the COF crystals embedded in GCOMx was evidenced by high resolution transmission electron microscopy (HRTEM), which exhibited highly ordered arrangements with independent diffraction direction (Figure 2 and Figure S21). The distance between adjacent lattice fringes is 3.31-3.34 Å, which is closed to the theoretical interlamellar spacing of COF-LZU1 (3.4 Å)/TpPa (3.7 Å)/NUS14 (3.5 Å).[34] Followingly, two-dimensional synchrotron radiation grazing incidence wide-angle X-ray scattering (GIWAXS) experiments of GCOMx verified the consistent orientation of COFs on the membrane surfaces. The projection of the GIWAXS data near $q_{xy} = 0$ indicated peaks at 1.6-2.0 $Å^{-1}$, corresponding to (001) reflection planes and π–π stacking of COF crystals in GCOMx.[35] As shown in Figure 3a,

the diffraction ring with high intensity represents a sharp (001) peak at the out-of-plane direction, suggesting the face-on orientations of COF crystals in GCOMx.[36] Thus, the three embedded COF crystals (i.e., COF-TpPa, COF-LZU1, COF-NUS14) adopt partial orientation in COF membranes as their channels (c axis) are not randomly directed but partly perpendicular to the membrane Top/Bottom surfaces. Powder X-ray diffraction (PXRD) further confirmed crystallinity of the COF crystals on GCOMx surfaces. Unlike amorphous porous PIL-M (Figure S22), GCOM1, GCOM2, and GCOM3 exhibited PXRD reflections with a first 2θ peak at low angles of 4.7°, 4.8° and 2.9°, respectively (Figure 3b). These peaks can be ascribed to the (100) reflection plane of COF crystals, while the broad peak at higher 2θ (~27°) is mainly due to the π–π stacking between the COF layers within GCOM1.[37] In general, the observed PXRD patterns for COF-TpPa, LZU1 and NUS14 in GCOMx matched well with the simulated patterns obtained using the eclipsed A-A stacking model (Figure S23-25). After soaking in different organic solvents for 24 hours, sharp PXRD patterns of COF-TpPa, COF-LZU1, COF-NUS14 still can be observed, demonstrating the stable crystallinity of the GCOMx in different solvents (Figure S26). Fourier transform infrared spectroscopy (FT-IR) was used to verify the chemical structures and internal interactions in GCOMx and PIL-M. As shown in Figure 3c, FT-IR spectra of PIL-M exhibited a red shift in the vibration band of the carboxylate groups from 1635 cm^{-1} to 1688 cm^{-1}, which can be ascribed to the deprotonated carboxylate groups in PIL-M[38] (Figure S27). The carbonyl (C=O) peak of GCOM1 broadens at 1685 cm^{-1} comparing to COF-TpPa, and merges with the peak for GCOM1's newly formed C=C bond (1578 cm^{-1}), which can be attributed to the strong hydrogen bonding in the keto form of honeycomb 2D framework and confirms the s-*cis* structure. The imine group (C=N) peak of GCOM2 (1621 cm^{-1}) and GCOM3 (1621 cm^{-1}) are both enhanced, indicating the formation of imine-linked covalent skeletons.[38] Furthermore, the structural integrity of GCOMx were verified by ^{13}C CP-MAS solid-state nuclear magnetic resonance (NMR) spectroscopy (Figure S28). In the NMR test, GCOM1 showed a signal at ~182 ppm that corresponds to the carbonyl carbon of the keto form,

while GCOM2, GCOM3 showed peaks at ~160 ppm and ~156 ppm that corresponds to the imine bonds of the frameworks[31] (Figure S27). The pore structures of GCOMx are characterized by N_2 adsorption-desorption isotherms (Figure S29). The Brunauer-Emmett-Teller (BET) surface areas were determined to be ~179, ~662, ~1012 $m^2 g^{-1}$ for COF powders from GCOM1, GCOM2, and GCOM3,[32] however, due to the large amount of PIL in the membrane, the specific surface areas of GCOMx (GCOM1: 83.5 $m^2 g^{-1}$, GCOM2: 98.4 $m^2 g^{-1}$, GCOM3: 48.2 $m^2 g^{-1}$) are greatly reduced. Hence, GCOMx possess wider pore size distributions centered at 1-2 nm, the minimum pore sizes of GCOMx are ~1.2 nm, ~1.4 nm, ~1.5 nm, respectively, determined by the nonlocal density functional theory (NLDFT) fitting (Figure S30). Meanwhile, GCOMx exhibited robustness and flexibility while bending or twisting (Figure S9d-f). The mechanical properties and flexibility of GCOMx were analyzed by tensile test, and the mechanical strength of GCOMx is 2-3 times higher than the original PIL-M (Figure 3d and Table S2). To conclude, the gradient distribution of COF crystals is beneficial to enhance the tensile strength of the membrane, in accordance to their natural gradient analogues, *e.g.,* bamboo stems[39] or shell nacre.[40] Compared with reported COF membranes,[41, 42] the COFs in GCOMx show a high crystallinity and the entire membrane exhibit good mechanical robustness even though they are produced under mild synthesis conditions. Briefly, owing to their pore uniformity, the GCOMx are certainly promising for solvent filtration applications. Besides, the thermogravimetric analyses (TGA) indicate that the PIL-M and GCOMx remain stable until 240 °C (Figure S31).

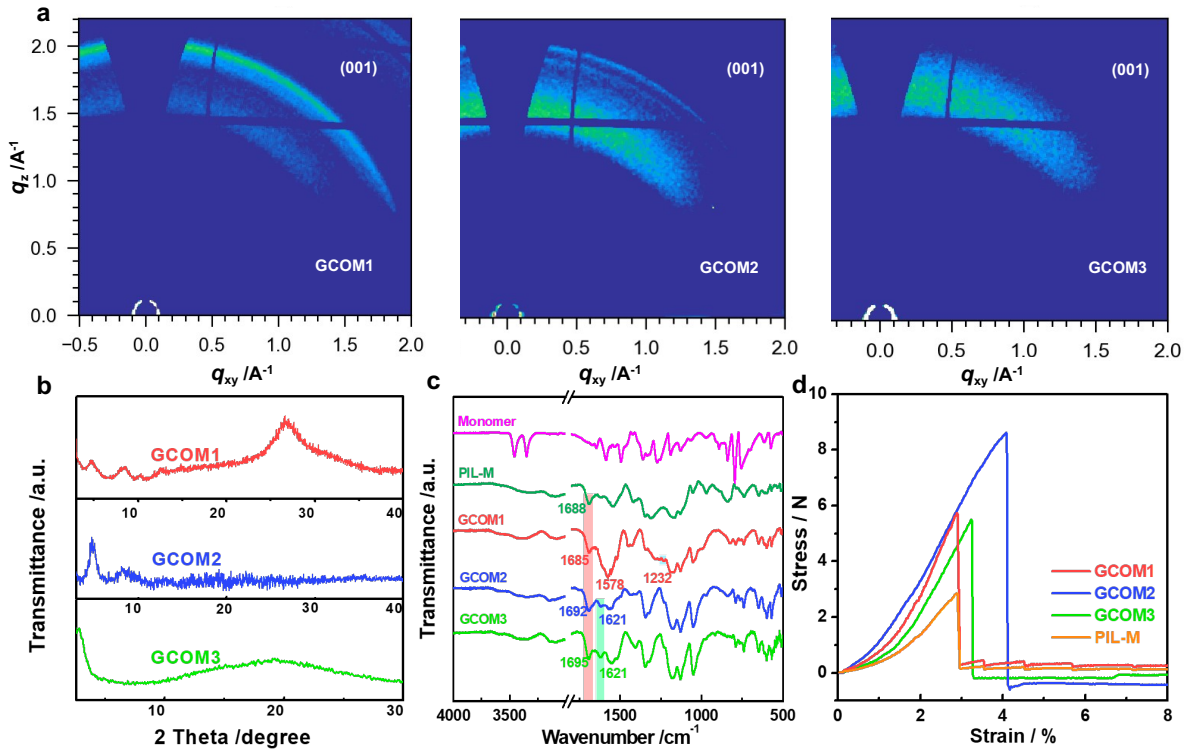

Figure 3. Crystallinity, structure, and mechanical property of GCOMx. a GIWAXS patterns of GCOM1, GCOM2, and GCOM3; **b** X-ray diffraction patterns of GCOM1, GCOM2, and GCOM3; **c** FT-IR spectra of monomer, PIL membrane (PIL-M), GCOM1, GCOM2, and GCOM3; **d** The stress-strain of GCOM1, GCOM2, GCOM3 and PIL-M.

3. Results and Discussion of GCOMx

3.1. Asymmetric solvent transport through GCOMx

The existence of graded distributed COF crystals inside membranes gave rise to an asymmetric solvent transport. In a typical run, the solvent permeation experiments carried out on GCOMx were kept at a consistent operating pressure of 2 bar. When the Bottom surface of GCOM1 was applied as the feed side and exposed to the solvent flow, the solvent permeance reaches up to 181.28 LMH bar^{-1} and 81.24 LMH bar^{-1} for methanol and ethanol, respectively (Figure 4a). By contrast, when the Top surface of GCOM1 was applied as the feed side and exposed to the solvent flow, the solvent permeance reaches merely at 10.34 LMH bar^{-1} and 8.44 LMH bar^{-1} for methanol and ethanol, respectively, which is one order of magnitude lower (10~18 times) than those of bottom surface feeding. This asymmetric solvent transport characteristic of GCOM1 can be interpreted by the permeability asymmetry factor (PAF), which is defined as

the ratio of the permeabilities measured in the two directions. Here, the PAF reached to 10~18 (bottom/top) for GCOM1. Furthermore, the rejection rate of azorubine (AR) for the Bottom surface as the feed side is almost equal to the Top surface in molecular sieving (Figure 4b). Meanwhile, as an intrinsic property, the organic solvent permeability of (homogeneous) membranes should not be influenced by their chemical properties.[43] Therefore, the asymmetric transportation of GCOM1 can only be ascribed to its gradient porous structures. In order to understand the asymmetric permeance phenomenon existing in GCOMx, a steady state flow field of microscopic flow state model with graded apertures was constructed using COMSOL Multiphysics software to simulate solvent permeation in GCOM1 (Figure 4c and Figure S32-33). The velocity and pressure distributions of the forward (bottom to top) and backward (top to bottom) flow field were obtained by applying equal positive and reverse pressure differences to the open boundary of both ends (Figure 4d). The overall volume flow in the case of forward and backward flow is calculated based on the *Navier-Stokes equation* (laminar flow)[44] (Table S3). As illustrated in the scheme, the solvent flow is calculated to be 4.59×10^{-6} μm^3 s^{-1} (forward) and 1.02×10^{-6} μm^3 s^{-1} (backward), respectively, exhibiting an obvious asymmetric fluid flow for the volume flow system. In detail, the fluid flow difference of the forward and backward model is 4.48, if the fuild flow difference increased linearly or exponentially, a hierarchy number of 1200 or 320 will be demanded for 10-fold flux difference for forward and backward models. Given this perspective, gradient structures with a hierarchy number reaching up to hundreds/thousands can lead to more than 10-fold flux difference, confirming the theoretical possibility of asymmetric fluid permeance caused by graded aperture structures, which agreed well with the experimental observations for GCOM1. Generally, from theoretical calculation, fluid flowing from large to small apertures resulted in faster permeation speed compared with its backward model. Alternatively, according to the *Bernoulli differential equation*[45] and Venturi effect,[46] the fluid velocity can be accelerated when passing through shrinking solvent

flow channels and vice versa. In extreme circumstances, an infinite hierarchical gradient porous structure may lead to an infinite fluid velocity or result in a nonflow system with forward and backward flux, respectively, revealing the possibility of GCOMx as unidirectional transportation membranes.

$$(\rho \frac{\partial u}{\partial t} + \rho(u \cdot \nabla)u = \nabla[-pl + \mathrm{K}] + \mathrm{F}) \quad (1)$$

$$(\rho \nabla \cdot u = 0) \quad (2)$$

$$(\mathrm{K} = \mu(\nabla u + (\nabla u)^T)) \quad (3)$$

Navier-Stokes correlation equation; ρ is the density (Kg m^{-3}); u is the velocity vector (m s^{-1}); p is pressure (Pa); K is the viscous stress tensor (Pa); F is the volume force vector (N m^{-3}). Meanwhile, the fluid flow in practical experiments are influenced by many other factors (*e.g.,* viscosity, density, and polarity of solvents, chemical/physical interactions of solvents with pore walls, *etc.*). Therefore, the PAF values may vary upon applying different solvents as the fluid in the same system. For example, the viscosity of ethanol is higher than that of methanol, which may lead to more internal frictions when filtrated by gradient membrane and result in varied PAF.

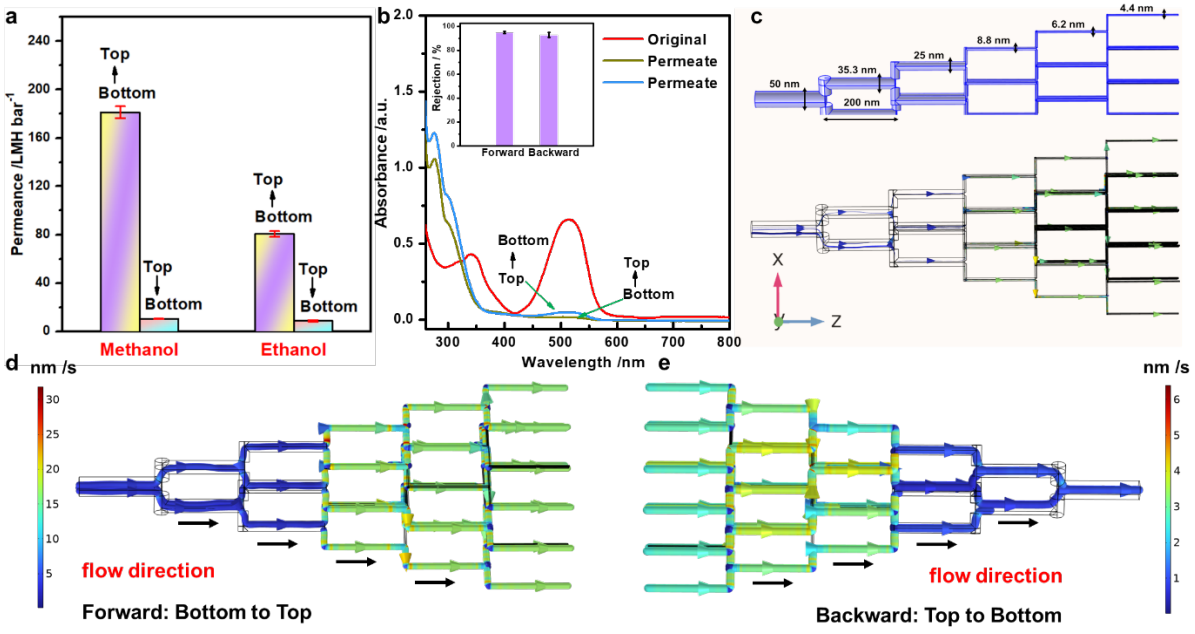

Figure 4. Asymmetric solvent transportation of GCOMx. a The methanol and ethanol flux of bottom and top side transport; **b** UV-vis spectra of AR in methanol for bottom and top side

sieving; **c** The microscopic flow state model of COMSOL Multiphysics; **d** Forward fluid field simulation of velocity; **e** Backward fluid field simulation of velocity.

3.2. Organic solvent nanofiltration performance of GCOMx

The OSN performance of GCOMx was evaluated based on crossflow filtration experiment with the bottom surface as the solvent feed side (crossflow filter shown in Figure S34). A series of methanol solutions with solutes spanning a range of molecular weights and sizes were applied in this work, and dyes are chosen as the organic micropollutants in solvents. The long-term OSN tests and ultraviolet-visible (UV-vis) absorption spectra of various dyes before and after filtration through GCOM1 and PIL-M are shown in Figure S35-36. It is worth noting that the short-end kinetic diameter of the 3D structure determines the effective size of the dye molecule, as illustrated in Figure S37. As expected, PIL-M with arbitrary large pores exhibited almost no rejection ability for dye molecules, except RB (rejection rate, 42.6 %) and BB-G (rejection rate, 28.1 %). In comparison, as can be seen in Figure S38, AR with a molecular weight of 502 g mol^{-1} and kinetic diameter of 1.12 nm was rejected by the GCOM1 (94.7 %). Meanwhile, GCOM2 and GCOM3 showed similar rejection behaviors during the OSN tests, with a clear molecular weight cut-off (MWCO) of 494, and 505 g mol^{-1}, respectively (Figure 5a, Table S4), exhibiting slightly lower dye rejections than GCOM1 (MWCO=472 g mol^{-1}). These results are consistent with the pore size differences between GCOM1, GCOM2, and GCOM3 (1.13 nm and 1.26 nm, Figure S31). COF pore channels are mainly responsible for molecular retention during dye separation. Figure 5b show a comparison of the performance of reported porous/polymer nanofiltration membranes with GCOMx (x=1,2,3), applying methanol as the solvent. As illustrated, the filtration performance of GCOM1 is superior to most reported POP membranes.[25, 47-53] In addition, the plot of MWCO versus rejection revealed that GCOMx possess an outstanding molecular sieving ability outperforming most COF membranes for OSN (Figure S39). Generally, the molecular sieving abilities of GCOMx are determined by multiple factors including solute size, solvent viscosity, solute-solvent interaction and aperture size of

the membrane.[54] Furthermore, the electrostatic interactions between the solute and membrane surface play an important role in aquatic nanofiltration.[48] As shown in Table S5, both sides of GCOM1, GCOM2, and GCOM3 exhibited negative zeta-potentials when tested in neutral environment (pH=7), with values of -6.60/-6.76, -4.26/-4.59, and -6.59/-6.83 mV (Top/Bottom), respectively. As a consequence, GCOM1 exhibited remarkable anionic dye sieving ability in aqueous solutions (Figure S40).

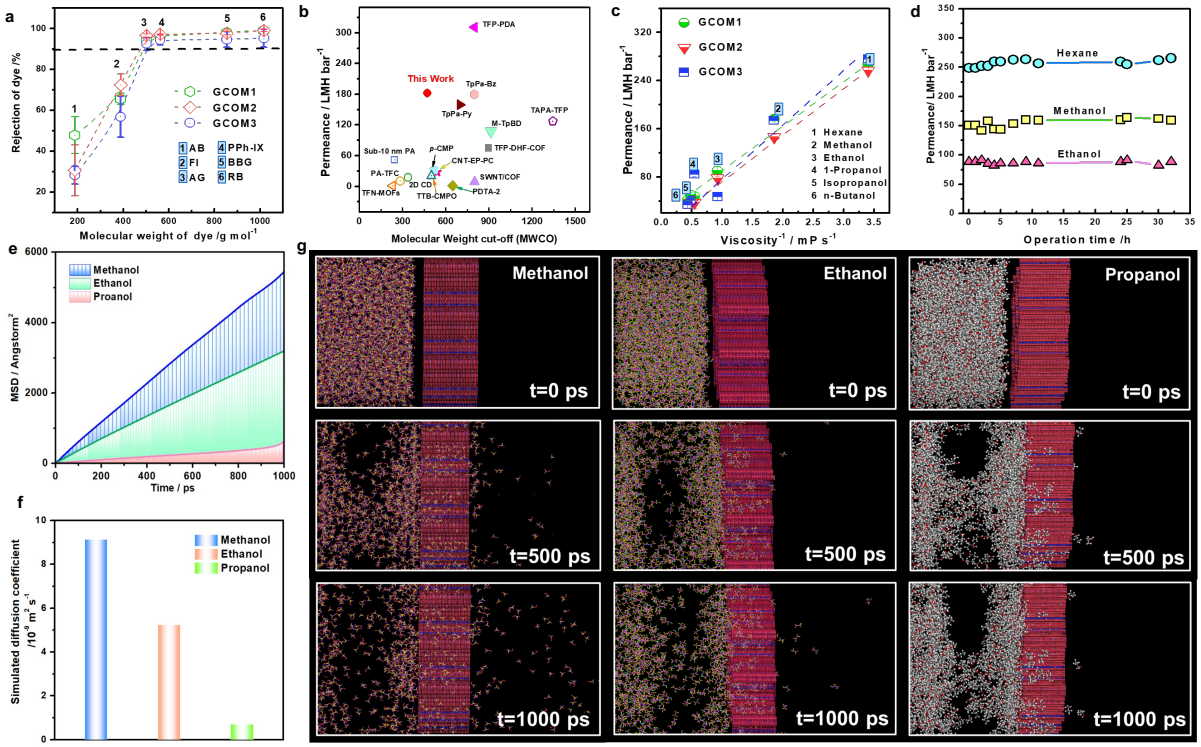

Figure 5. Solvent transport mechanism of GCOMx. a Dye molecules rejection of different GCOMx (x=1,2,3); **b** Permance-rejection performance comparison of GCOM1 with reported best-performing nanofiltration membranes. **c** Permeance-viscosity relationship of GCOM1, GCOM2, and GCOM3; **d** Long-term filtration test of hexane, methanol and ethanol on the GCOM1; **e** MSD of various solvents through GCOM1; **f** The simulated diffusivity of different solvents through GCOM1; **g** Simulation snapshots at 0, 500, 1000 ps for the three diffusion systems of methanol, ethanol and 1-propanol, respectively.

The permeation properties of different organic solvents through GCOMx were also systematically investigated. As shown in Figure S41, the solvent flux of 6 organic solvents (polar and nonpolar) at a pressure difference of 2 bar is plotted, along with their viscosities. In brief, solvent permeance increased inversely proportional to viscosity (1/μ) at the same pressure

(Figure 5c), suggesting that no specific interactions existed between varied solvents with hydrophobic pores in GCOMx.[55] Notably, the ethanol flux through GCOM1 corresponding to the permeance increased linearly with applied pressures (Figure S42). These results validated the assumption that pore flow could be obtained in GCOM1 with regular pore channels.[56] The OSN performance of GCOMx was also compared with other porous membranes including CMPs,[57] polyacrylate,[58] PIMs,[59] MOF composite[60] and inorganic OSN membranes, as listed in Table S6. In general, solvent permeances increased inversely proportional to membrane thicknesses. However, the methanol flux of GCOM1 still reaches 175.93 LMH bar^{-1} with a thickness of 40 μm, exceeding most COFs membranes (Figure S43 and Table S7).[61] Meanwhile, the thickness of polyamide-based nanofiltration membrane (52.2 LMH bar^{-1}) is 10 nm.[62] In other words, the OSN permeance of GCOM1 is two orders of magnitude (>100 times) faster than commercial polyamide OSN membrane, *i.e.*, DuraMem DM150 (0.48 LMH bar^{-1}, operating at 20 bar). This highly efficient solvent permeance and effective solute separation performance was correlated to the intrinsic microporosity of GCOMx.[63] Alternatively, the graded distributed COF crystals in GCOMx generated a broad active separation layer, who gradually aggregated from loose packings to dense layers across the membrane cross-sections. As such, the regular micropores in COFs along with gradient distribution of COF crystals from Top to Bottom of GCOMx led to a graded separation of target solutions, and eventually resulted in an efficient solute rejection with a high solvent flux, acting as a biomimetic high-efficiency filter.[64]

In addition to molecule rejection and solvent flux, permeance stability tests are also conducted for evaluating OSN performance of GCOMx. As illustrated in Figure 5d and Figure S44, the permeance stabilities of GCOMx were demonstrated applying several typical organic solvents, including polar and nonpolar ones. As can be seen in Figure S45, for the long-term stability test, tiny amounts of dyes adsorbed on the pore walls of GCOM1 caused a slight decrease (~8%) in permeability over the first 5 h. After that, GCOM1 manifested long-term stable permeance and

high rejection rate during continuous filtration test in methanol for 10 days. Then the tested GCOM1 was cleaned up and no blockage was observed (Figure SS46). As expected, the permeabilities of GCOMx were highly stable in various organic solvents, including methanol, ethanol, acetone, tetrahydrofuran, toluene and DMF (Figure S47). Moreover, the organic solvent tolerance of the GCOMx was verified by SEM. As shown in Figure S48, morphologies of the GCOMx remained unaltered after OSN test, demonstrating their excellent chemical and structural stability. Evidently, incorporation of the COF crystals into the polymer substrates endows GCOMx excellent mechanical/chemical stability, along with remarkable permeability. In consideration of the aforementioned chemical structures and experimental analyses, the permeation behavior of GCOMx can be estimated. With hydrophilic pore channels decorated by -OH moieties and polar N─H and C═O covalent bonds at the pore walls, GCOM1 exhibited a water contact angle of 27°, much smaller than that of GCOM2 (119°) and GCOM3 (123°) (Figure S49). GCOM1 exhibited an enhanced water flux than GCOM2 and GCOM3 due to their difference in hydrophilicity (Figure S50). As a result, it exhibited more favorable affinity toward polar solvents comparing with GCOM2 and GCOM3. Therefore, GCOM1 exhibits a higher methanol flux than GCOM2 and GCOM3 as well as lower hexane flux than GCOM2 and GCOM3 (Figure 5d, Figure S44). Comparing to the solvent permeances by solution-diffusion transport through the dense DuraMem membrane, these COF composite membranes exhibited significantly higher permeances resulting from their pore flow transport.[65] Specifically, the transport mechanism of solution-diffusion model depends on the molecular structure of the solvents, membrane porosity, and chemical affinity between solvents and pore surfaces of the membranes.[66, 67] Dense membranes have strong solvent-membrane interaction which resulted in high transport resistance and low fluxes.[68] On the contrary, porous membranes like GCOMx possessed abundant porosity but are lack of solvent-membrane interaction, which endowed them high fluxes with low transport resistance.[50]

3.3. Theoretical approach on GCOMx molecular permeability

To get deep insight into the solvent filtration behavior of GCOM1, molecular models were applied to simulate COF structures as separating layers for OSN. The crystallographic details of COF models are given in the Supplementary Methods (Figure S51, Table S8-10).[31, 32] Factors including single regular channels, pass-through, viscosities of solvents and interactions between solvents and membranes are expected to cause different solvent flow rate.[56] To verify the assumption, continuous 1-propanol, methanol and ethanol flow through the micropores of GCOM1 were simulated by polymer congruent field of force (PCFF).[69] Solvent-permeation rate of GCOM1 was evaluated according to the MSD. As shown in Figure 5e, the MSD of different solvents follows the order of $MSD_{methanol} > MSD_{ethanol} > MSD_{1\text{-propanol}}$. The simulated diffusion coefficient of methanol, ethanol, 1-propanol was calculated to 9.13, 5.24, 0.69×10^{-9} $m^2\ s^{-1}$, respectively (Figure 5f). Specifically, at the beginning of the calculation, no molecules were present at the permeate side of the GCOM1 membrane along the z-direction in the system. After 500 ps, plenty of methanol but few ethanol and 1-propanol molecules can be found on the permeate side. The difference of diffusion rate between molecules is more obvious when the movement time reaches 1 ns. This indicates that the diffusion rate of methanol was much faster than that of ethanol and 1-propanol through the GCOM1 (Figure 5g), being consistent with the experiments. Notably, it can be observed that solvent molecules moved constantly in the system and exhibited vibrations with small amplitudes in most cases, which further proved that the pore channels of GCOM1 possess an excellent molecular sieving ability. In brief, the simulation results matched well with experiments.

3.4. High-efficiency Biomolecule Cleaning Device

Separation and purification of effective ingredients from crude pharmaceutical products or Chinese herbal medicine is of great significance for pharmaceutical production. In order to obtain high-purity raw materials/active pharmaceutical ingredients (API) that meet the pharmaceutical standards, membrane separations are intensely involved.[70] Nevertheless, achieving efficient separation of API/medicines with small molecular weights ($\leqslant$1000 g mol^{-}

[1]) demands separation membranes with precise pore apertures, such as GCOMx. Thus, to demonstrate the practical separating performance of GCOM1, a mixed drugs filtration through GCOM1 was performed under a constant operating pressure of 2 bar. Herein, two small molecular medicines, ofloxacin (OLA) and azithromycin (AZM), are chosen as the testing targets due to their commercial availability and comparable molecular weights. Notably, both medicines are difficult to be removed from medical wastewater and of high-value to be isolated for recycling, owing to their broad-spectrum antibacterial activity.[71] The long-term filtration studies were conducted with a feed solution containing equal concentrations of OLA and AZM in methanol. Crossflow filtration was applied to avoid membrane contamination induced by concentration polarization. After 24 h filtration, it is found that GCOM1 rejected 98.3% of AZN and 60.1% of OLA, respectively, as determined by UV-vis absorption of the filtrate (Figure 6a). Upon the separation difference between OLA and AZM, pure OLA can be acquired through several filtering circulation. As such, with the separation ability of GCOMx for pharmaceuticals, combining their asymmetric solvent transport behavior, such membranes possess huge potentials for industrial separation/purification/circulation of pharmaceutical molecules Furthermore, to explore the potential implication scope of GCOMx, a simulated kidney dialysis was conducted through filtration experiments. In the experiment, a simulated composition of human blood, with protein (globulin; ovalbumin), bilirubin, glucose, urea and uric acid as the solute, methanol and water as the solvent, respectively, was filtered and collected for comparison (Figure 6b). Upon analysis, the filtrated "raw urine" contained 52 mg L^{-1} (in methanol)/48 mg L^{-1} (in water) urea and 82 mg L^{-1} (in methanol)/46 mg L^{-1} (in water) uric acid, with no protein, glucose or bilirubin components detected (Table S11 and Table S12), verified the effectiveness of GCOMx as simulated dialysis membranes. Additionally, this simulated dialysis was tested applying Bottom and Top surface of the membrane as the solvent feed side, respectively. It is worth noting that, the forward and backforward operation of such simulated dialysis exhibit an obvious different solvent permeation of 113.2 LMH bar^{-1} (Bottom

to Top) and 19.5 LMH bar^{-1} (Top to Bottom), repectively, demonstrating the ability of GCOMx as bionic backflow prevention dialysis membranes. Moreover, GCOMx exhibit a high flux during the simulated dialysis, surpassing conventional hemofiltration membranes (Table S13).[72] To sum up, this asymmetric dialysis function of GCOMx is of vital importance for recontamination prevention in biological areas as well as industry fields.[73, 74]

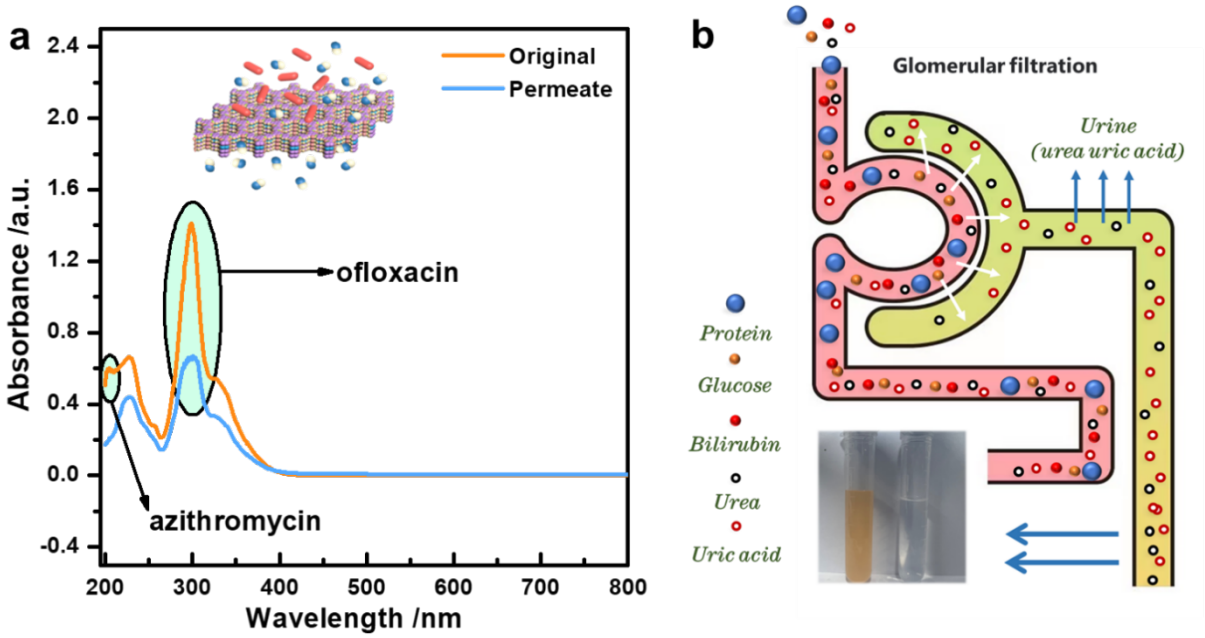

Figure 6 Drug separation and simulated kidney dialysis. a UV-vis absorption spectra of a mixture (ofloxacin, azithromycin) solution (methanol) before and after the filtration through the GCOM1; **b** Simulated renal tubular dialysis of blood.

4. Conclusion

In summary, a universal approach for constructing gradient covalent organic framework membranes was developed *via* applying porous poly(ionic liquid) membrane as template. The fabricated GCOMx exhibited excellent permeances in nonpolar (hexane~260.45 LMH bar^{-1}) and polar (methanol~175.93 LMH bar^{-1}) solvents, with narrow MWCO (472 g mol $^{-1}$) and MWRO (<182 g mol^{-1}). Importantly, GCOMx exhibited an asymmetric solvent transport when applying different membrane side as the solvent feed surface during filtration, verified by theoretical calculation with hydromechanical prediction model. The fluids obtained from

membrane surfaces with large and sparse apertures to the ones with dense and small pores resulted in a more efficient flowing (10~18 times) comparing with its reverse operation. This finding demonstrates a disruptive understanding for structure-function relations of gradient structure with fluid flow, and, in our opinion, opens a new design paradigm based on "gradient induced asymmetric solvent flow". Afterwards, GCOMx were examined for mixed drug separation and simulated kidney dialysis, resulting in high effectiveness. Such gradient porous membranes provide a powerful toolbox for advanced membrane technology, many interesting concerted practices can be applied with such designable gradient structures, *e.g.,* as biodialyzer for unidirectional separation and purification of biologic agents, and our cognition of gradient membranes can be updated.

5. Experimental Section/Methods

5.1. Synthesis of poly(ionic liquid)s

Poly[3-cyanomethyl-1-vinylimidazolium bis(trifluoromethane sulfonyl)imide] (simplified as "PImi") was synthesized according to method of reference[28]. The chemical structures were proven by ^{1}H NMR spectra in Figure S1.

5.2. Synthesis of PIL membrane (PIL-M)

34 mg 0.17 mmol of DAPAC was dissolved in 8 mL of DMSO. Subsequently, 140 mg 0.34 mmol of PIL was added and dissolved. The mixture solution was stirred for 6 h, and after that, it was cast onto a circular glass vessel. Then the solution mixture was put into an oven and heated for 8 h at 80 °C. Then the dry PIL-M, which is stick to the circular glass vessel, was immersed into an aqueous solution of 0.25 wt % ammonia for 2 h. The membrane was washed with deionized water for several times and then peeled off from the circular glass vessel for further use. The PIL-M were immersed into different organic solvents and aqueous solutions with different pH values for two weeks at room temperature. The digital images show no structural damages for all these membranes. (Figure S52)

5.3. Synthesis of GCOMx

The preparation methods of GCOM1, GCOM2 and GCOM3 were comparable and are documented in detail in the supplementary information.

5.4. Nanofiltration measurements

The membranes were sealed into a cross-flow filtration cell for permeance and rejection tests under a pressure of 2 bar. The effective filtration diameter of membranes in this device was 1 cm, supported by a porous stainless-steel disc. The selected GCOMx membrane was fixed at the bottom of the membrane pool. Filter paper was applied as a protective layer. The temperature of the feed solution in all experiments was maintained at 25 °C. Before permeance tests, the membranes were pre-pressed at a crossflow pressure of 2 bars for at least 30 min to obtain a stable permeance. The organic solvent flux and permeance (P, LMH bar^{-1}) of the membrane were calculated using the following equation:

$$J = V/(S \times t) \quad (4)$$

$$P = J/\Delta P \quad (5)$$

where V is the volume of the organic solvent, S is the effective membrane area, t is the experimental time and ΔP is the experiment pressure, respectively.

Different molecular concentrations of 30 ppm in organic solvents or 30 ppm in aqueous solution were determined using an ultraviolet visible (UV-vis) spectrometer at least two times. The rejection R (%) was calculated using the equation:

$$R = \left(1 - \frac{C_p}{C_f}\right) \times 100\% \quad (6)$$

where C_p and C_f are the solute concentrations of the permeate and feed, respectively.

5.5. Hydromechanical simulation

The phase-field modeling in this work is a typical hydromechanical model for microchannel fluid problem. All flow fields are based on the CFD module in COMSOL Multiphysics software. Based on the exponential type (level five, 1/32) geometric model, the simulation steady state

flow field of microchannel is constructed. The microchannel model is divided into two types. The forward channel model has a large hole at the beginning of the opening end, and the aperture decreases step-by-step. The opening end of the reverse runner model possess a small aperture, which increases step-by-step. By applying equal positive and reverse pressure difference to the open boundary of both ends, nonlinear Navier slip, the velocity and pressure distributions of the whole flow field are obtained. The overall volume flow rates in the case of forward and backward flow are obtained as well.

5.6. Simulation of solvent flow through GCOM1

All molecular dynamics calculations were performed on the Materials Studio (MS) program. In this study, the layer number (n) of membranes was set to 20 and the end groups were saturated by H atoms. Firstly, an aggregation with four layers of covalent organic framework models was selected to build the membrane using crystal cell modules. The solvent (methanol, ethanol, 1-propanol) flow through the GCOM1 was simulated with the model generated in the main context with cell dimension. The three-dimensional box was 67.668 × 67.668 × 70 Å at a density of 0.8 g cm^{-3}, the layer/GCOM1 periodic slabs were separated by a vacuum region. The molecule was described with PCFF. The Discover module was used to simulate NVT dynamics at 298 K. A time step of 1 fs was used. The COF active layer kept fixed in the whole simulation process.

Supporting Information

Supporting Information is available from the Wiley Online Library or from the author.

Acknowledgements

The authors gratefully acknowledge the supports from the National Key Research and Development Program of China (2022YFB3807100, 2022YFB3807102, 2022YFB3807103), the Fundamental Research Funds for the Central Universities (2232022A-03), the National Natural Science Foundation of China (22102021, 52073046, 52373172, 22375037), the

Program of Shanghai Academic Research Leader (21XD1420200), the Chang Jiang Scholar Program (Q2019152), the Natural Science Foundation of Shanghai (23ZR1401100 and 21ZR1402700) for the financial supports. We thank beamline BL16B1 at Shanghai Synchrotron Radiation Facility (SSRF) for the GIWAXS experiment.

Received: ((will be filled in by the editorial staff))
Revised: ((will be filled in by the editorial staff))
Published online: ((will be filled in by the editorial staff))

References

[1] A. Kamtsikakis, J. Baales, V. V. Zeisler-Diehl, DD. Vanhecke, J. Zoppe, O. L. Schreiber, C. Weder, *Nat. Commun.* **2021**, *12*.

[2] Y. Ge, K. Liu, G. Yang, X. Yu, B. Sun, B. Zhang, Y. Yuan, M. Zeng, N. Wang, C. Xing, H. Mao, *Renal Failure* **2022,** *44*, 2037-2045.

[3] J. H. Miner, *Pediatr. Nephrol.* **2011**, *26*, 1413-1417.

[4] P. M. Beringer, H. Owens, A. Nguyen, N. Mordwinkin, S. Louie, SM. Mak, F. Sattler, *Pharmacotherapy.* **2010**, *30*, 1004-1010.

[5] H. D. Humes, D. Buffington, A. Westover, S. Roy, W. H. Fissell, *Pediatr Nephrol* **2014**, *29*, 343-351.

[6] J. B. Fan, J. Luo, Z. Luo, Y. Song, Z. Wang, J. Meng, B. Wang, S. Zhang, Z. Zheng, X. Chen, S. Wang, *ACS Nano.* **2019**, *13*, 8374-8381.

[7] S. Zhao, C. Jiang, J. Fan, S. Hong, P. Mei, R. Yao, Y. Liu, S. Zhang, H Li, H. Zhang, C. Sun, Z. Guo, P. Shao, Y. Zhu, J. Zhang, L Guo, Y. Ma, J. Zhang, X. Feng, F. Wang, H. Wu, B. Wang, *Nat. Mater.* **2021**, *20*, 1551-1558.

[8] S. Gao, J. Chen, Y. Zheng, A. Wang, D. Dong, Y. Zhu, Y. Zhang, W. Fang, J. Jin, *Adv. Funct. Mater.* **2022**, *32*, 2205990.

[9] H. Yang, H. Wu, Z. Yao, B. Shi, Z. Xu, X. Cheng, F. Pan, G. Liu, Z. Jiang, X. Cao, *J. Mater. Chem. A* **2018**, *6*, 583-591.

[10] Q. Zhao, J. W. Dunlop, X. Qiu, F. Huang, Z. Zhang, J. Heyda, J. Dzubiella, M. Antonietti, J. Yuan, *Nat. Commun.* **2014**, *5*, 4293.

[11] G. Bian, N. Pan, Z. Luan, X. Sui, W. Fan, Y. Xia, K. Sui, L. Jiang, *Angew. Chem. Int. Ed.* **2021**, *60*, 20294-20300.

[12] E. Kanzawa, S. Aoyagi, T. Nakano, *Mater. Sci. Eng. C* **2011**, *31*, 1050-1054.

[13] F. Ansari, A. Sjöstedt, P. T. Larsson, A. Berglund, L. Wågberg, *Part A Appl. Sci. Manuf.* **2015**, *74*, 60-68.

[14] Y. Li, W. Chen, G. Xing, D. Jiang, L. Chen, *Chem. Soc. Rev.* **2020**, *49,* 2852-2868.

[15] S. B. Yu, H. Lyu, J. Tian, H. Wang, D. W. Zhang, Y. Liu, Z. T. Li, *Poly. Chem.* **2016**, *7*, 3392-3397.

[16] X. Wang, X. Han, J. Zhang, X. Wu, Y. Liu, Y. Cui, *J. Am. Chem. Soc.* **2016**, *138*, 12332-12335.

[17] R. Sun, S. Hou, C. Luo, X. Ji, L. Wang, L. Mai, C. A. Wang, *Nano Letters* **2020**, *20*, 3880-3888.

[18] Z. Li, Y. Zhang, H. Xia, Y. Mu, X. Liu, *Chem. Commun.* **2016**, *52*, 6613-6616.

[19] H. Y. Zuo, Y. Li, Y. Z. Liao, *ACS Appl. Mater. Interfaces* **2019**, *11*, 39201-39208.

[20] N. Huang, P. Wang, D. L. Jiang, *Nat. Rev. Mater.* **2016**, *1,* 16068.

[21] M. Xu, X. Zhu, J. Zhu, S. Wei, X. Cong, Z. Wang, Q. Yan, L. Weng, L. Wang, *Nanotechnology* 2023, *34,* 1361-1382 (2023).

[22] Y. X. Sun, J. Zhao, X. Z. Li, H. Jiang, Y. J. Cai, X. Yang, Y. Liu, Y. B. Li, Z. H. Yang, Y. G. Wu, L. Y. Chen, J. G. Gai, *ACS Appl. Mater. Interfaces* **2023**, *15*, 18550-18558.

[23] D. W. Burke, C. Sun, I. Castano, N. C. Flanders, A. M. Evans, E. Vitaku, D. C. McLeod, R. H. Lambeth, L. X. Chen, N. C. Gianneschi, W. R. Dichtel, *Angew. Chem. Int. Ed.* **2020**, *59*, 5165-5171.

[24] S. Hou, W. Ji, J. Chen, Y. Teng, L. Wen, L. Jiang, *Angew. Chem. Int. Ed.* **2021**, *60*, 9925-9930.

[25] S. Kandambeth, B. P. Biswal, H. D. Chaudhari, K. C. Rout, S. Kunjattu, S. Mitra, S. Karak, A. Das, R. Mukherjee, U. K. Kharul, R. Banerjee, *Adv. Mater.* **2017**, *29*, 1603945.

[26] Q. Zhao, M. Yin, A. P. Zhang, S. Prescher, M. Antonietti, J. Y. Yuan, *J. Am. Chem. Soc.* 2013, *135*, 5549-5552.

[27] M. M. Pendergast, E. M. V. Hoek, *Energy Environ. Sci.* **2011**, *4*, 1946-1971.

[28] J. K. Sun, H. J. Lin, W. Y. Zhang, M. R. Gao, M. Antonietti, J. Y. Yuan, *Mater. Horizons* **2017**, *4*, 681-687.

[29] Y. C. Yuan, B. Sun, A. M. Cao, D. Wang, L. J. Wan, *Chem. Commun.* **2018**, *54*, 5976-5979.

[30] F. Para, F. Bocquet, L. Nony, C. Loppacher, M. Féron, F. Cherioux, D. Z. Gao, F. Federici Canova, M. B. Watkins, *Nat. Chem.* **2018**, *10*, 1112-1117.

[31] S. Y. Ding, J. Gao, Q. Wang, Y. Zhang, W. G. Song, C. Y. Su, W. Wang, *J. Am. Chem. Soc.* **2011**, *133*, 19816-19822.

[32] B. P. Biswal, S. Chandra, S. Kandambeth, B. Lukose, T. Heine, R. Banerjee, *J. Am. Chem. Soc.* **2013**, *135*, 5328-5331.

[33] Y. Peng, W. K. Wong, Z. Hu, Y. Cheng, D. Yuan, S. A. Khan, D. Zhao, *Chem. Mater.* **2016**, *28*, 5095-5101.

[34] Y. Ying, S. B. Peh, H. Yang, Z. Yang, D. Zhao, *Adv. Mater.* **2022**, *34*, 2104946.

[35] X. He, Y. Yang, H. Wu, G. He, Z. Xu, Y. Kong, L. Cao, B. Shi, Z. Zhang, C. Tongsh, K. Jiao, K. Zhu, Z. Jiang, *Adv. Mater.* **2020**, *32*, 2001284.

[36] H. Yang, R. Zhang, L. Wang, J. Zhang, X. Yu, J. Liu, R. Xing, Y. Geng, Y. Han, *Macromolecules* **2015**, *48*, 7557-7566.

[37] S. Yuan, X. Li, J. Zhu, G. Zhang, P. Van Puyvelde, B. Vander Bruggen, *Chem. Soc. Rev.* **48** 2665-2681.

[38] C. Qian, W. Zhou, J. Qiao, D. Wang, X. Li, W. L. Teo, X. Shi, H. Wu, J. Di, H. Wang, G. Liu, L. Gu, J. Liu, L. Feng, Y. Liu, S. Y. Quek, K. P. Loh, Y. Zhao, *J. Am. Chem. Soc.* **142** 18138-18149.

[39] Y. Wang, H. Wang, Y. Chen, C. Srinivasakannan, R. Tang, X. Duan, *J. Porous Mater.* **2022**, *30*, 671-680.

[40] X. Wang, X. Jiang, H. Sun, Y. Zhang, Y. Fang, R. Shu, *Mater. Charact.* **2022***, 193*, 112307.

[41] T. Liu, L. Cui, H. Zhao, X. Zhang, *ACS Appl. Mater. Interfaces* **2020**, *12*, 47090-47098.

[42] Y. He, X. Lin, J. Chen, Z. Guo, H. Zhan, *ACS Appl. Mater. Interfaces* **2020**, *12***,** 41942-41949.

[43] K. Prasad, M. Nikzad, I. Sbarski, *J. Polym. Res.* **2018**, *25*, 232.

[44] H. Koch, D. Tataru, *Adv. Math (N Y).* **2001**, *157*, 22-35.

[45] A. Chandra, D. Pathiwada, S. Chattopadhyay, *Chem. Eng. Res. Des.* **2019**, *142*, 386-411.

[46] R. Gentle, P. Edwards, B. Bolton, *Butterworth-Heinemann: Oxford* **2001**, *3*, 112-168.

[47] Z. Zhou, X. Li, D. Guo, D. B. Shinde, D. Lu, L. Chen, X. Liu, L. Cao, A. M. Aboalsaud, Y. Hu,Z. Lai, *Nat. Commun.* **2020**, *11*, 5323.

[48] X. Shi, Z. Zhang, S. Fang, J. Wang, Y. Zhang,Y. Wang, *Nano Letters* **2021**, *21*, 8355-8362.

[49] K. Dey, M. Pal, K. C. Rout, S. Kunjattu H, A. Das, R. Mukherjee, U. K. Kharul,R. Banerjee, *J. Am. Chem. Soc.* **2017**, *139*, 13083-13091.

[50] D. B. Shinde, G. Sheng, X. Li, M. Ostwal, A. H. Emwas, K. W. Huang, Z. Lai, *J. Am. Chem. Soc.* **2018**, *140*, 14342-14349.

[51] N. Manoranjan, F. Zhang, Z. Wang, Y. Dong, W. Fang, Y. Zhang, Y. Zhu,J. Jin, *ACS Appl. Mater. Interfaces* **2020**, *12*, 53096-53103.

[52] X. Lai, C. Wang, L. Wang, C. Xiao, *J. Water Process.Eng.* **2022**, *45*, 102533.

[53] N. A. Khan, R. Zhang, H. Wu, J. Shen, J. Yuan, C. Fan, L. Cao, M. A. Olson, Z. Jiang, *J. Am. Chem. Soc.* **2020**, 142, 13450-13458.

[54] R. Shevate, D. L. Shaffer, *ACS Nano* **2022**, *16*, 2407-2418.

[55] S. Karan, S. Samitsu, X. Peng, K. Kurashima, I. Ichinose, *Science* **2012**, *335*, 444-447.

[56] J. Liu, G. Han, D. Zhao, K. Lu, J. Gao,T. S. Chung, *Sci. Adv.* **2021**, *6*, eabb1110.

[57] X. He, H. Sin, B. Liang, Z. A. Ghazi, A. M. Khattak, N. A. Khan, H. R. Alanagh, L. Li, X. Lu, Z. Tang, *Adv. Funct. Mater.* **2019**, *29*, 1900134.

[58] M. F. Jimenez-Solomon, Q. Song, K. E. Jelfs, M. Munoz-Ibanez, A. G. Livingston, *Nat. Mater.* **2016**, *15*, 760-767.

[59] P. Marchetti, M. F. Jimenez Solomon, G. Szekely, A. G. Livingston, *Chem. Rev.* **2014**, *114*, 10735-10806.
[60] S. Sorribas, P. Gorgojo, C. Téllez, J. Coronas, A. G. Livingston, *J. Am. Chem. Soc.* **2013**, *135*, 15201-15208.
[61] B. Liang, H. Wang, X. Shi, B. Shen, X. He, Z. A. Ghazi, N. A. Khan, H. Sin, A. M. Khattak, L. Li, Z. Tang, *Nat. Chem.* **2018**, *10*, 961-967.
[62] S. Karan, Z. Jiang, A. G. Livingston, *Science* **2015**, *348*, 1347-1351.
[63] M. Galizia, K. P. Bye, *Front. Chem.* **2018**, *6*, 51-60.
[64] S. Ling, Z. Qin, W. Huang, S. Cao, D. L. Kaplan, M. J. Buehler, *Sci. Adv.* **2017**, *3*, e1601939.
[65] L. Wang, M. S. H. Boutilier, P. R. Kidambi, D. Jang, N. G. Hadjiconstantinou,R. Karnik, *Nat. Nanotechnol.* **2017**, *12*, 509-522.
[66] Y. Li, Q. Wu, X. Guo, M. Zhang, B. Chen, G. Wei, X. Li, X. Li, S. Li, L. Ma, *Nat. Commun.* **2020**, *11*, 599.
[67] R. Wang, X. Shi, A. Xiao, W. Zhou, Y. Wang, *J. Membr. Sci.* **2018**, *566*, 197-204.
[68] L. Xia, J. R. McCutcheon, *Sep. Purif. Technol.* **2020**, *238*, 116398.
[69] Z. Zhou, D. Guo, D. B. Shinde, L. Cao, Z. Li, X. Li, D. Lu, Z. Lai, *ACS Nano* **2021**, *15*, 11970-11980.
[70] L. Peeva, J. D. Burgal, I. Valtcheva, A. G. Livingston, *Chem. Eng. Sci.* **2014**, *116*, 183-194.
[71] Z. L. Mthiyane, N. Makhubela, H. Nyoni, L. M. Madikizela, B. R. Maseko, S. Ncube, *Environ. Techno.* **2023**, *3*, 1-31.
[72] D. F. Stamatialis, B. J. Papenburg, M. Gironés, S. Saiful, S. N. M. Bettahalli, S. Schmitmeier, M. Wessling, *J. Membr. Sci.* **2008**, *308*, 1-34.
[73] E. D. Den Aantrekker, W. W. Vernooij, M. W. Reij, M. H. Zwietering, R. R. Beumer, M. Van Schothorst, R. M. Boom, *J. Food Protect.* **2003**, *66*, 1432-1438.
[74] Q. Liu, Y. Zhang, W. Liu, L. H. Wang, Y. W. Choi, M. Fulton, S. Fuchs, K. Shariati, M. Qiao, V. Bernat, M. Ma, *Adv. Funct. Mater.* **2021**, *31*, 2103477.